



Fabrication of $(\text{TiZrNbSiMo})_{1-x}\text{N}_x$ high entropy alloy coatings using a high power impulse magnetron sputtering technique: Effects of nitrogen addition

Bih-Show Lou ^{a,b}, Ren-Zong Lin ^c, Chia-Lin Li ^d, Jyh-Wei Lee ^{c,d,e,f,*}

^a Chemistry Division, Center for General Education, Chang Gung University, Taoyuan, Taiwan

^b Department of Orthopaedic Surgery, New Taipei Municipal TuCheng Hospital, Chang Gung Memorial Hospital, Taiwan

^c Department of Materials Engineering, Ming Chi University of Technology, New Taipei, Taiwan

^d Center for Plasma and Thin Film Technologies, Ming Chi University of Technology, New Taipei, Taiwan

^e College of Engineering, Chang Gung University, Taoyuan, Taiwan

^f High Entropy Materials Center, National Tsing Hua University, Hsinchu, Taiwan



ARTICLE INFO

Keywords:

High entropy alloy coatings

HIPIMS

Nitrogen content

Electrical resistivity

Corrosion resistance

ABSTRACT

Due to the outstanding mechanical and physical properties of high entropy alloy (HEA) coatings, the global academic and industrial communities have made significant research efforts in recent years, aiming to expand their industrial applications. In this study, TiZrNbSiMo and $(\text{TiZrNbSiMo})_{1-x}\text{N}_x$ HEA nitride coatings with different nitrogen contents were fabricated using a high power impulse magnetron sputtering (HIPIMS) system. By varying the nitrogen flow rates, the nitrogen contents of coatings increased from 0 to 48.8 at. %. The deposition rate decreased with increasing nitrogen content due to the target poisoning effect. Very fine and dense microstructure can be seen for each coating. The amorphous structure was obtained as the nitrogen content was lower than 19.1 at.%, whereas a nanocrystalline FCC structure was formed when the nitrogen content reached 34.9 at. %. Furthermore, the corrosion resistance of TiZrNbSiMo and four TiZrNbSiMoN HEA coatings in 0.5 M H_2SO_4 aqueous solution were superior to uncoated 304 stainless steel. We can conclude that the nanocrystalline TiZrNbSiMoN HEA coatings with a nitrogen content of 34.9 at. % exhibited a high hardness of 15.6 GPa, an electrical resistivity of 766.5 $\mu\Omega\cdot\text{cm}$, and an excellent corrosion polarization resistance of $9.71 \times 10^5 \Omega\cdot\text{cm}^2$, 610.7 times higher than 304SS. This study provides valuable insights for future promising applications of $(\text{TiZrNbSiMo})_{1-x}\text{N}_x$ HEA nitride coatings in severely corrosive environments, such as the protective coatings on stainless steel bipolar plates in proton exchange membrane fuel cells.

1. Introduction

In 2004, the invention of high entropy alloys (HEAs) [1] and equiatomic multicomponent alloys [2] have revolutionized the traditional concept of alloys by no longer considering each metal in the alloy as a primary constituent; instead, multiple elements are regarded as equally important components. Soon, the concept of HEA and multi-component alloys gained widespread attention in academia and were developed through various preparation methods such as arc melting, casting, powder metallurgy, etc. In recent years, high entropy alloy coatings have become a research focus, which can be deposited by cathodic arc deposition, ion sputtering, and magnetron sputtering methods [3–5]. High entropy alloy nitride coatings have attracted

extensive attention and research due to their high hardness [6], wear resistance [6,7], thermal stability [8], corrosion resistance [9], and radiation resistance [10].

In general, the BCC-structured high entropy alloy coatings exhibit lower hardness. Strong metal-nitrogen bonds can be formed in the coatings with the proper amount of reactive nitrogen gas added to increase its lattice distortion and solid solution strengthening effects [11–14]. Lai et al. [11] investigated the impact of nitrogen flow rates on the phase structure and mechanical properties of AlCrTaTiZr nitride coatings. It was observed that as the nitrogen content increased, the AlCrTaTiZr nitride changed from an amorphous phase to a face-centered cubic (FCC) phase. The AlCrTaTiZr N_x coatings exhibited the highest hardness of 32 GPa at a nitrogen flow rate of 14 %, corresponding to a

* Corresponding author at: Department of Materials Engineering, Ming Chi University of Technology, New Taipei, Taiwan.

E-mail address: jefflee@mail.mcut.edu.tw (J.-W. Lee).

nitrogen content of 50 at.%. However, the hardness gradually decreased to 27 GPa as the nitrogen flow rate increased to 60 % and the nitrogen content in the coatings still exceeded 50 at.%. Li et al. studied (NbTa-MoW)_{1-x}N_x high entropy nitride films [13] and found that as the nitrogen gas flow rate increased from 2.5 % to 5 %, the nitrogen content in the film increased from 7.84 to 12.47 at.%. The hardness gradually increased from 25.6 GPa for the nitrogen-free coating to 30.8 GPa at a nitrogen content of 29.81 at.%. However, the hardness decreased to 20 GPa as the nitrogen content was further increased to 39.37 at.%. The correlation between nitrogen content and mechanical properties in HEA nitride coatings is significantly different from typical transition metal nitrides such as TiN, TiAlN and TiAlSiN, where the nitrogen content must be approximately 50 at.% to achieve the highest hardness. For instance, in TiAlSiN films, the nitrogen composition needs to be close to 50 at.% to achieve the maximum hardness of 42 GPa [15]. In contrast, HEA nitride films have an optimum nitrogen content of 20–30 at.%, achieving the highest hardness. Further, a higher nitrogen content results in a decrease in film hardness, suggesting a possible correlation with the target poisoning issue [11,12,16–19]. There have been numerous studies on the effect of nitrogen flow rate on the phase structure and mechanical properties of HEA nitride coatings, such as (MoSiTiVZr)N_x [20], (AlCrTiZrHf)N [21], (AlCrTiZrV)N_x [22], (TiNbZr)N [23], (TiHfNbZrTa)N [24], (TiZrNbTaFe)N [16], (NbTaMoW)N [19] and (WNbTaTi)N [14]. We can conclude that the increasing nitrogen contents can accelerate the formation of the nitride phase and greatly improve the hardness and elastic modulus of coatings [11,12,14,16,19–22].

Fuel cell technology is very important because of its ability to solve the worldwide pollution threats and provides the future energy demands. Proton exchange membrane fuel cells (PEMFCs) are the key component for the electric vehicle powered by hydrogen, which is a replacement of the conventional internal combustion engines car. Since >30 % of the total fuel cell cost and around 70 % of the total weight of a PEMFC is graphite bipolar plate, the replacement of expensive graphite bipolar plates becomes a critical issue. In general, the AISI 316 L stainless steel exhibits excellent conductivity, high corrosion resistance and good mechanical properties. However, the strong sulfuric acid environment in the PEMFC environment still has a strong corrosion attack on the 316 L SS. Through proper surface engineering, bipolar plates can be protected by carbide coating [25] and HEA nitride coating [26] to enhance its corrosion resistance and prolong the lifespan application in hydrogen powered fuel cell vehicles.

The HiPIMS technology, known for its high power density, allows for the generation of elevated discharge current and plasma density, surpassing conventional direct current (DC), medium frequency (MF), and radio frequency (RF) magnetron sputtering systems [27]. This unique capability in HiPIMS facilitates highly dissociative sputtering of the target material [28], resulting in deposited coatings with denser and smoother microstructures [27,29]. In this study, (TiZrNbSiMo)_{1-x}N_x HEA coatings with different nitrogen contents were prepared using the HiPIMS system. The effects of nitrogen concentrations on the phase, microstructure, mechanical properties, electrical resistivity and corrosion resistance of coatings were thoroughly investigated. The possible applications of the (TiZrNbSiMo)_{1-x}N_x HEA coatings as the protective layer grown on the stainless steel plate against 0.5 M H₂SO₄ aqueous solution was discussed.

2. Experimental procedure

This study employed a high power impulse magnetron sputtering, HiPIMS, system to deposit five (TiZrNbSiMo)_{1-x}N_x HEA coatings with varying nitrogen contents on P-type (100) silicon wafers and AISI304 stainless steel (304SS) plate substrates. The equimolar TiZrNbSiMo HEA target, produced through powder metallurgy, was connected to the HiPIMS system operating at a frequency of 500 Hz and a 3 % duty cycle. A second titanium target, powered by a DC power source, was used to

Table 1
Deposition parameters of (TiZrNbSiMo)_{1-x}N_x HEA coatings.

Sample designation	N0	N2	N4	N6	N10
HIPIMS power of HEA target (W)	800				
HIPIMS frequency (Hz)	500				
HIPIMS duty cycle (%)	3				
Input Ar gas (sccm)	50	48	46	44	40
Input N ₂ gas (sccm)	0	2	4	6	10
N ₂ gas ratio (%)	0	4	8	12	20
Substrate DC bias (V)		−50			
Substrate temperature (°C)		200			

deposit an interlayer between HEA coatings and substrates. Each target had a diameter of 152.4 mm. The HiPIMS power for the HEA target was maintained at 800 W, and the nitrogen gas flow was varied from 0, 2, 4, 6, to 10 sccm to obtain five (TiZrNbSiMo)_{1-x}N_x HEA coatings with different nitrogen contents.

Prior to coatings deposition, the vacuum chamber was evacuated to 8×10^{-4} Pa, and a 10-min etching process was conducted using 50 sccm of argon gas flow and 2.0 Pa of working pressure at a substrate bias voltage of −800 V. Another 10 min deposition of a Ti interlayer at 500 W using a DC power source under 0.4 Pa of working pressure and 50 sccm argon flow was performed before the growth of (TiZrNbSiMo)_{1-x}N_x HEA coatings. The Ti interlayer was deposited to improve the adhesion property of HEA coating on the substrates. The distance between the target and the substrate was maintained at 27 cm. During the deposition process, the substrate holder rotated at a speed of 10 rpm to ensure the uniformity of the chemical composition. Table 1 provides detailed deposition conditions and sample designations for five (TiZrNbSiMo)_{1-x}N_x HEA coatings.

The chemical compositions of five (TiZrNbSiMo)_{1-x}N_x HEA nitride coatings grown on silicon wafers were analyzed using a field emission electron probe microanalyzer (FE-EPMA, JXA-iHP200F, JEOL, Japan). The coating's crystal structure was examined using X-ray diffraction analysis with a grazing incidence X-ray diffraction instrument (GIXRD, Empyrean, PANalytical, The Netherlands) at 30 kV and 40 mA with an incidence angle of 1°. Surface morphology and average surface roughness (Ra) of the coatings on silicon wafers were analyzed using an atomic force microscope (AFM, Dimension Edge, Bruker, USA). Cross-sectional morphology of each coating was observed using a field emission scanning electron microscopy (FE-SEM, JSM-6701, JEOL, Japan). The samples for transmission electron microscopy (TEM) analysis were prepared using a focused ion beam system (Hitachi NX2000, Japan). A TEM (JSM-2100, JEOL, Japan) was conducted for detailed phase and microstructure analysis of selected coatings. A four-point probe tester (NAP-RT-70/RG-7B, Napson Corp., Japan) was used to measure the electrical resistivity measurements of HEA coatings.

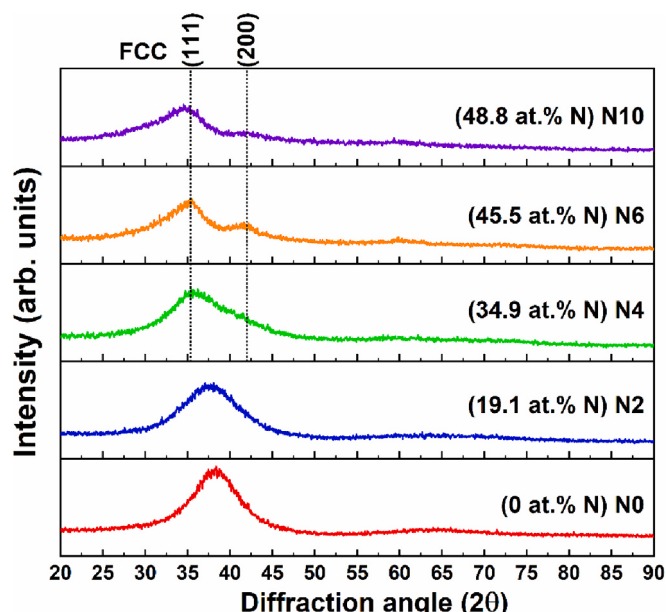
The hardness and reduced elastic modulus of the coatings grown on silicon wafers were measured using a nanoindenter (TI-950 Triboindenter, Bruker, USA) with a Berkovich 142.3° diamond probe tip (tip radius ≤ 50 nm). This test comprised a minimum of eight indents spaced 15 μm away, with a fixed indentation depth of 60 nm (constant depth mode). The area function of the nanoindenter was calibrated using a fused quartz standard sample. Software was employed to compensate for the thermal drift effect of the nanoindenter. The laser curvature method for determining the residual stress values of five coatings grown on Si wafer substrates were determined using Stoney's equation [30]:

$$\sigma_f = \left[\frac{M_s}{6(1 - v_s)} \right] \left(\frac{t_s^2}{t_f} \right) \left(\frac{1}{R} - \frac{1}{R_0} \right) \quad (2)$$

where σ_f is the residual stress of coating, v_s is the Poisson's ratio (0.279) [31] of the Si substrate, t_s is the thickness of Si substrate (525 μm), t_f is thickness of coating, M_s is the biaxial modulus of the Si substrate (130.2 GPa), and R_0 and R are the radii of curvature of the Si substrate before

Table 2Chemical composition and configurational entropy of $(\text{TiZrNbSiMo})_{1-x}\text{N}_x$ coatings.

Sample	x	Composition (at. %)							ΔS_{mix}
		Ti	Zr	Nb	Si	Mo	N	O	
N0	0	21.6 ± 0.3	15.3 ± 0.1	16.6 ± 0.2	21.8 ± 0.1	18.5 ± 0.1	0	6.2 ± 0.2	1.60R
N2	0.19	18.4 ± 0.5	12.2 ± 0.1	13.3 ± 0.2	18.2 ± 0.2	14.9 ± 0.1	19.1 ± 0.6	3.9 ± 0.2	1.59R
N4	0.35	14.4 ± 0.3	9.6 ± 0.1	9.9 ± 0.2	15.9 ± 0.1	11.5 ± 0.1	34.9 ± 0.1	3.8 ± 0.2	1.59R
N6	0.46	12.0 ± 0.2	7.5 ± 0.1	8.1 ± 0.1	14.9 ± 0.1	9.1 ± 0.1	45.5 ± 0.2	2.9 ± 0.2	1.58R
N10	0.49	10.8 ± 0.1	6.3 ± 0.1	7.3 ± 0.1	14.9 ± 0.0	8.5 ± 0.2	48.8 ± 0.5	3.4 ± 0.1	1.56R

**Fig. 1.** X-ray diffraction patterns of five $(\text{TiZrNbSiMo})_{1-x}\text{N}_x$ HEA coatings.

and after the coating deposition, respectively. The BK7 glass plates with curvatures of 0, 0.1, -0.1, 0.2, and -0.2 m⁻¹ were used as calibration standards. The deviation of residual stress was kept within 10 %.

Finally, the corrosion resistance of the coating deposited on 304SS substrates in 0.5 M H₂SO₄ aqueous solution was evaluated by the potentiodynamic polarization test using an electrochemical workstation

(SP-200, Biologic, France). During the corrosion test, nitrogen gas was continuously introduced until the end of the test. A three-electrode system, including a silver/silver chloride (Ag/AgCl) reference electrode, a platinum auxiliary electrode and working electrode was used. Prior to the potentiodynamic polarization test, we stabilized the corrosion set-up by measuring open circuit potential (OCP) for 30 min. Thereafter, the potentiodynamic polarization tests were studied in an applied potential range from -0.5 V to +2 V versus the open circuit potential at a scanning rate of 0.5 mV/s. The corrosion resistance of uncoated 304SS was also evaluated as a reference.

3. Results and discussion

3.1. Chemical composition of $(\text{TiZrNbSiMo})_{1-x}\text{N}_x$ HEA coatings

Table 2 lists the chemical compositions and mixing entropy values for each coating. It can be found that with an increase in nitrogen gas flow from 0 to 2 and 4 sccm, the nitrogen content rises rapidly from 0 to 19.1 and further to 34.9 at.%. The nitrogen concentration increases from 45.5 to 48.8 at.% as the nitrogen gas flow increases from 6 to 10 sccm. Based on the chemical composition of nitrogen-free N0 coating, it is not an equimolar concentration possibly because of the difference of sputtering yields for each element. The higher contents of Si and Ti around 21.6 to 21.8 at.% and a relatively lower Zr concentration of 15.3 at.% can be seen in **Table 2**. It is noticed that the high oxygen content of 6.2 at.% can be seen in the N0 coating possibly due to the oxygen residual in the HEA target and the contamination form the deposition chamber. In the nitrogen containing coatings, the contents of all elements decrease with increasing nitrogen content. The mixing entropy for each coatings can be calculated using the following equation [32]:

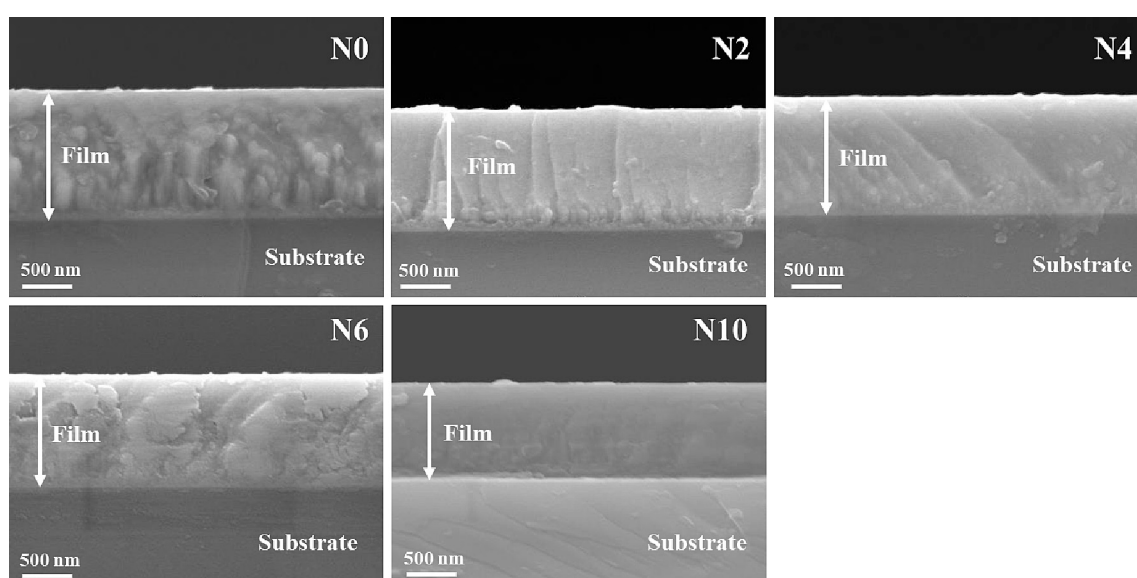
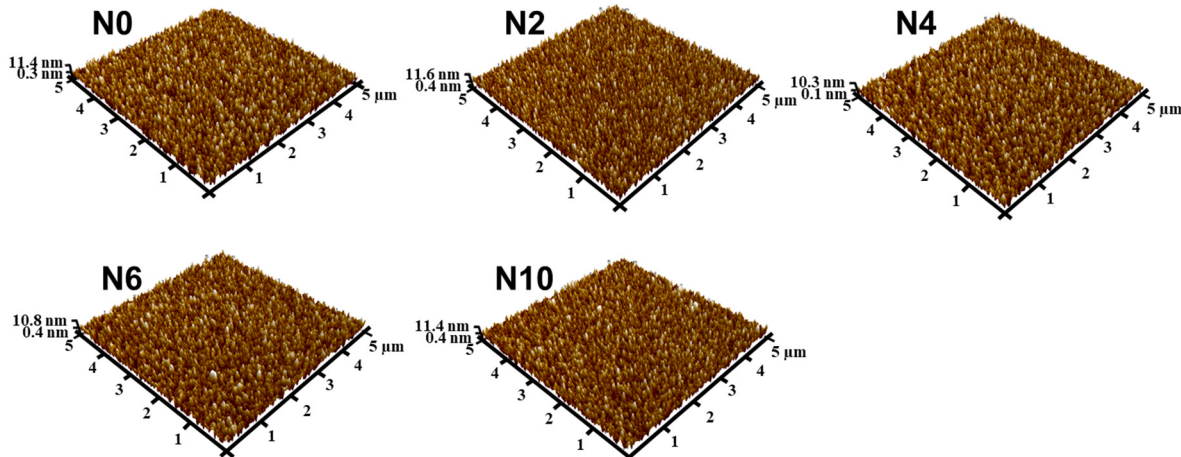
**Fig. 2.** Cross-sectional FE-SEM image of five coatings.

Table 3

Characteristics of five HEA coatings.

Sample designation	N0	N2	N4	N6	N10
N (at. %)	0	19.1	34.9	45.5	48.8
Thickness (nm)	1168.7 ± 9.5	1063.7 ± 13.7	1059.3 ± 11.7	1021.3 ± 5.7	928.4 ± 3.8
Deposition rate (nm/min/kW)	8.59	7.82	7.79	7.51	6.83
Roughness, Ra (nm)	2.47 ± 0.15	2.37 ± 0.22	2.24 ± 0.14	2.27 ± 0.12	2.35 ± 0.15
Hardness, H (GPa)	9.7 ± 0.2	15.4 ± 0.3	15.6 ± 0.3	15.4 ± 0.3	14.0 ± 0.4
Reduced elastic modulus, E _r (GPa)	145 ± 2	172 ± 1	176 ± 1	173 ± 1	163 ± 1
H/E _r	0.067	0.090	0.089	0.089	0.086
H ³ /E _r ² (GPa)	0.043	0.123	0.123	0.122	0.103
Residual stress (GPa)	0.43 ± 0.04	0.01 ± 0.03	-0.09 ± 0.08	-0.19 ± 0.04	-0.35 ± 0.04
Electrical resistivity (μΩ·cm)	214.2 ± 2.3	249.4 ± 3.1	766.5 ± 8.3	2322.9 ± 24.7	3147.8 ± 11.3

**Fig. 3.** AFM surface topography images of five HEA coatings.

$$\Delta S_{mix} = -R \sum_{i=1}^n (x_i \ln x_i) \quad (1)$$

where R is the gas constant ($8.314 \text{ J}\cdot\text{mol}^{-1}\cdot\text{K}^{-1}$), n is the number of components, and x_i is the atomic percentage of component i . Based on the calculated values as listed in Table 2, the mixing entropy values (ΔS_{mix}) decrease gradually with increase nitrogen content, which are all higher than $1.5R$, implying all coatings satisfy the definition of high entropy alloys.

3.2. Microstructure of $(\text{TiZrNbSiMo})_{1-x}\text{N}_x$ HEA coatings

Fig. 1 depicts the X-ray diffraction patterns of five $(\text{TiZrNbSiMo})_{1-x}\text{N}_x$ HEA coatings. It is evident that N0 and N2 exhibit an amorphous structure, while coatings with nitrogen content higher than 34.9 at. % (N4 and others) reveal the typical B1 face-centered cubic (FCC) (111) and (200) peaks. For the N2 coatings containing 19.1 at. % nitrogen and 18.2 at. % silicon, the amorphous-like structure is observed due to the formation of amorphous silicon nitride phase. We observed a phase transition from amorphous to nanocrystalline FCC structure within the nitrogen content range from 19.1 to 34.9 at. %, which is consistent with our previous studies [16]. Subsequent confirmation of these observations will be provided through the TEM analysis.

Very dense cross-sectional microstructure is shown in Fig. 2 for each $(\text{TiZrNbSiMo})_{1-x}\text{N}_x$ HEA coating. The average thickness values of coatings (as listed in Table 3) decrease from 1168.7 to 928.4 nm and the average deposition rate decreases from 8.59 to 6.83 nm/min as the nitrogen content increases from 0 to 48.8 at.%, which can be attributed to the target poisoning effect [12,14,16,17,19,21].

Fig. 3 displays the AFM surface morphologies of $(\text{TiZrNbSiMo})_{1-x}\text{N}_x$ HEA coatings. Very flat and fine microstructure can be seen for each coating. The average surface roughness is ranging from 2.24 to 2.47 nm as listed in Table 3. Notably, there is no noticeable effect on surface

roughness resulting from nitrogen content or phase structure.

The cross-sectional TEM bright-field images and selected area electron diffraction (SAED) patterns of N0 and N2 coatings are depicted in Fig. 4(a) and (d). No crystalline phases or nanograins can be observed in the TEM images. For the high-resolution TEM images of N0 and N2 samples, as shown in Figs. 4 (c) and (d), a maze and random structure can be seen. The inserted fast Fourier transform (FFT) images also show the halo ring patterns, indicating their amorphous nature, which are consistent with the XRD result in Fig. 1.

For N4 coating, a low magnification TEM image, the SAED pattern, corresponding dark field images of (111) plane and a high-resolution TEM (HRTEM) image were displayed in Fig. 5. Based on the SAED pattern in Fig. 5(b), the diffraction rings can be indexed as (111), (200) and (220) reflections of the FCC nanocrystalline structure. The size distribution of these nanocrystallites can be inferred to be at least $<5 \text{ nm}$ in diameter from the dark-field images of the (111) planes in Fig. 5(c). The HRTEM image in Fig. 5(d) shows no obvious lattice fringe feature, but only a small short-range ordering can be identified, as indicated by the white dashed circles. It can be confirmed that the N4 coating results in a nanocomposite microstructure consisting of very fine nanocrystallites embedded in the amorphous matrix.

The low magnification TEM image, SAED pattern, corresponding dark field images of the (111) and (200) planes and a HRTEM image are shown in Fig. 6 for the N6 coating containing 45.5 at.% nitrogen. As compared with the N4 coating as depicted in Fig. 5(b), the diffraction rings of the SAED pattern in Fig. 6(b) are much clearer and easier to index as (111), (200) and (220) reflections of the FCC nanocrystalline structure, due to its higher nitrogen content and a greater amount of transition metal nitride phases. The dark-field images of the (111) and (200) planes in Figs. 6(c) and (d) show the distribution of the nanocrystallites, in which the amount of nanocrystallites was obviously higher than that of the N4 coating. Fig. 6(e) depicts an HRTEM image of

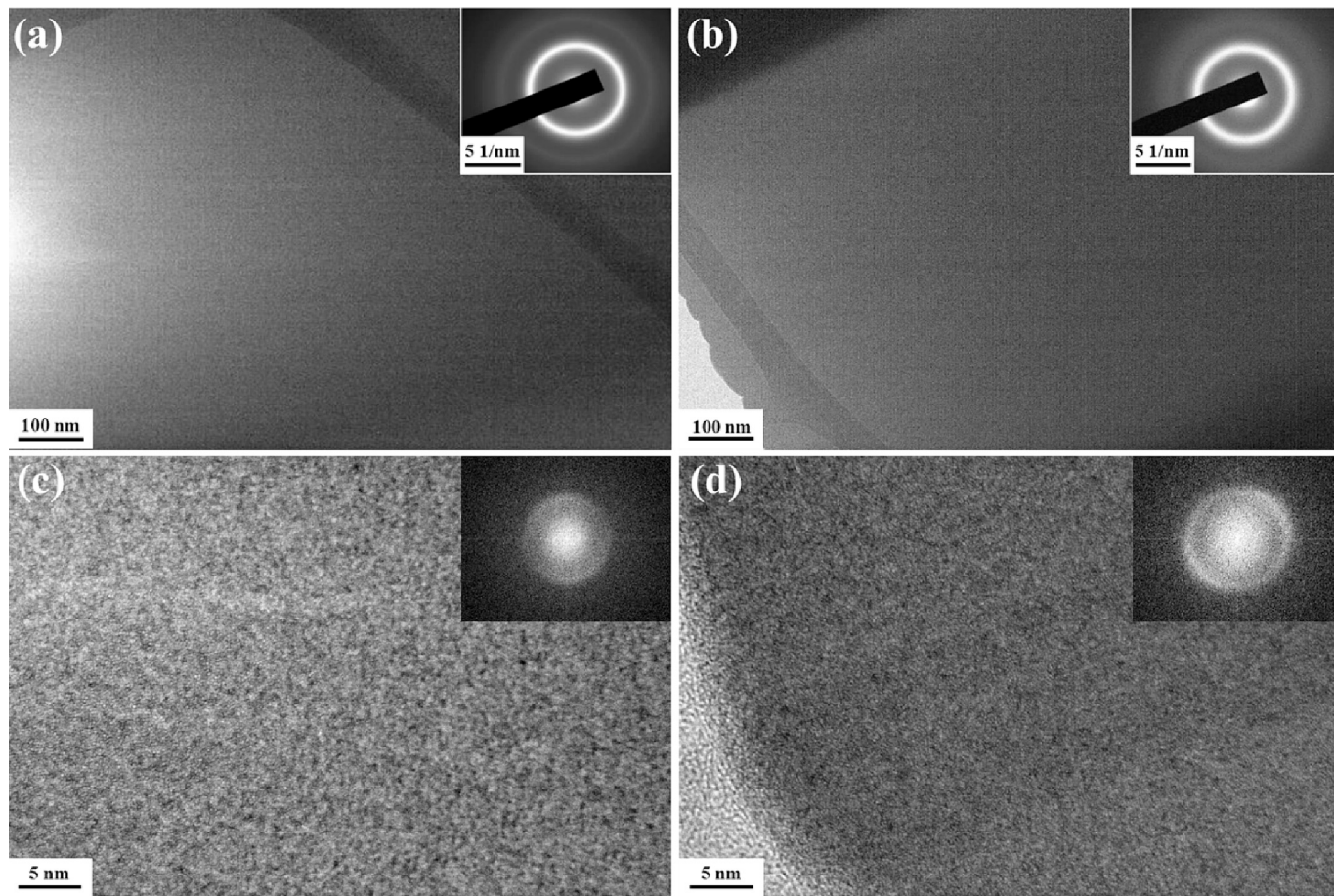


Fig. 4. The cross-sectional TEM bright field images and selected area electron diffraction patterns for (a) N0, (b) N2, as well as the high-resolution TEM images with corresponding fast Fourier transform (FFT) patterns for (c) N0, and (d) N2 coatings.

the N6 coating with the lattice fringes of d -spacing values approximately 0.202 nm, which is consistent with the typical d -spacing of FCC (111) plane. As compared with the nanocrystalline microstructures circled in Fig. 5(d) for N4 and Fig. 6(e) for the N6, the nanocrystallites for N6 coating are clearly to be seen due to its higher nitrogen content and more nitride crystallites.

Fig. 7(a) shows a low magnification TEM image for the N10 coating. The diffraction rings of FCC (111), (200) and (220) reflections of nanocrystalline structure in Fig. 7(b) can be identified. The two dark field images of (111) and (200) planes in Fig. 7(c) and (d) confirm the very fine nanograins microstructure in N10 coating. A few lattice fringes embedded in the amorphous matrix can be seen in the HRTEM image of Fig. 7(e), as indicated by the white dashed circles, and it can be concluded that the N10 coating was found to show less crystallinity than the N6 coating. This can be attributed to the fact that a higher nitrogen concentration in the N10 coating may lead to the formation of an amorphous silicon nitride phase more easily than in other coatings. This phenomenon can also be seen in other studies [33,34].

On the basis of XRD and TEM analysis results, the nitrogen-free TiZrNbSiMo HEA coating is amorphous structure. When the nitrogen content is at a lower level, such as 19.1 at.% or lower in this work, the nitrogen atoms may be located in the interstitial sites and have no influence on the crystallization of $(\text{TiZrNbSiMo})_{1-x}\text{N}_x$ HEA coatings, thereby retaining the amorphous structures. As the nitrogen content increases to a higher concentration, the nitrogen atoms react with Ti, Zr, Nb, Mo, and Si elements and transform into the FCC crystal structure. This increased nitrogen contents, 34.9 at.% in this work, leads to the nucleation and subsequent growth of FCC grains, resulting in the transition from an amorphous to an FCC nanocrystalline structure.

3.3. Mechanical property of $(\text{TiZrNbSiMo})_{1-x}\text{N}_x$ HEA coatings

Detailed information on the hardness, reduced elastic modulus and residual stress of $(\text{TiZrNbSiMo})_{1-x}\text{N}_x$ HEA coatings are given in Table 3. Fig. 8 illustrates the relationships between hardness, reduced elastic modulus and nitrogen content. For the nitrogen-free N0 coatings, the hardness is 9.7 GPa. As the nitrogen content increases to 34.9 at.%, the hardness of the coatings increases from 9.7 to 15.6 GPa due to the formation of transition metal nitride phases and solid solution strengthening of the various elements [21]. However, the hardness drops to 14 GPa as the nitrogen content further increases to 48.8 at.%. It is important to point out that the relatively lower hardness of these $(\text{TiZrNbSiMo})_{1-x}\text{N}_x$ HEA coatings than those reported in literature [11,12,19–22] is due to the formation of large amount of soft amorphous silicon nitride phase in this work. Yan et al. [10] reported that high entropy films (HEFs) present outstanding mechanical properties, with the incorporation of nitrogen and other elements contributing to a further improvement in the hardness of HEFs. Our previous study on TiZrNbTaFeN_x HEA coatings also found that adding nitrogen significantly increased the hardness of HEA coatings from 9.9 to 36.2 GPa as the nitrogen content increased from 0 to 32.0 at.% [16]. A similar hardness enhancement effect by adding nitrogen has been reported in the literature [11,12,16–19]. However, the hardness further decreases to a lower value as the nitrogen content is higher than a critical point, which is frequently reported in the nitrogen-contained HEA coatings [16,18,19,21]. This hardness-decreasing tendency is attributed to target poisoning, where the transition shifts from reactive sputtering from the metal target to a direct sputtering of nitride layers adhered on the poisoned target surface, resulting in the reduced hardness [21].

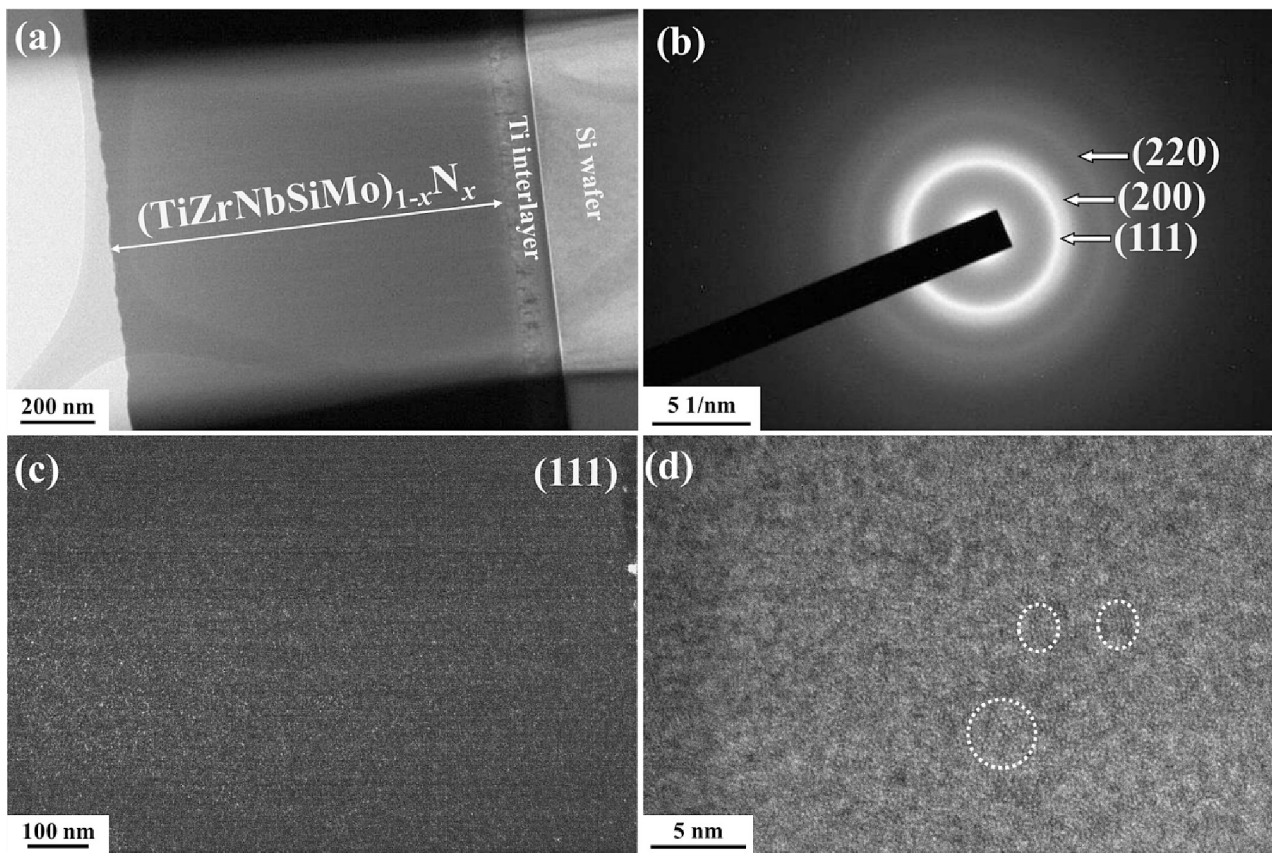


Fig. 5. The cross-sectional TEM (a) low magnification image, (b) selected area electron diffraction pattern, (c) dark field images of (111), and (d) high magnification image for N4 coating.

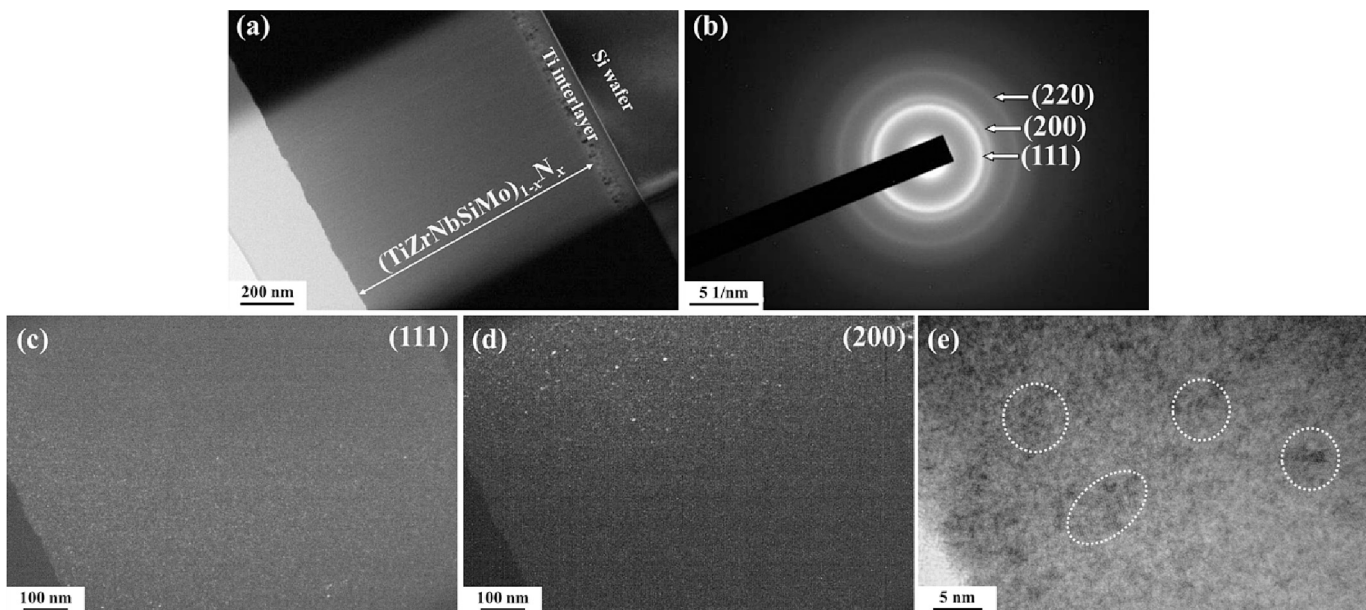


Fig. 6. The cross-sectional TEM (a) low magnification image, (b) selected area electron diffraction pattern, dark field images of (c) (111), (d) (200), and (e) high magnification bright field image for N6 coating.

The relationship between residual stress and nitrogen content is also illustrated in Fig. 8. The N0 coating exhibits a residual tensile stress of +0.43 GPa, and a near stress-free status (+0.01 GPa) can be achieved as increasing the nitrogen content to 19.1 at.-% (N2 coating). According to the study of $(\text{AlCrTaTiZr})\text{N}_x$ high entropy alloy nitride coatings [35], the

addition of nitrogen resulted in the formation of a nanocomposite structure consisting of nitride crystallites imbedded in the amorphous metallic matrix when the nitrogen level fell below 50 at.-%. The formation of nitride crystallites decreases the volume expansion brought by the short-range atomic order, which lowers the residual stress since

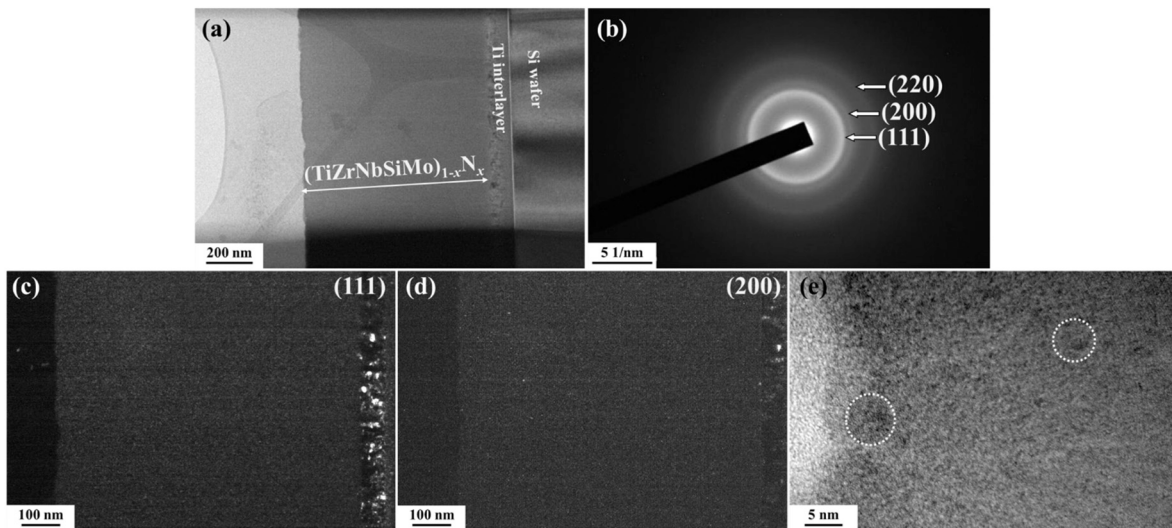


Fig. 7. The cross-sectional TEM (a) low magnification image, (b) selected area electron diffraction pattern, dark field images of (c) (111), (d) (200), and (e) high magnification bright field image for N10 coating.

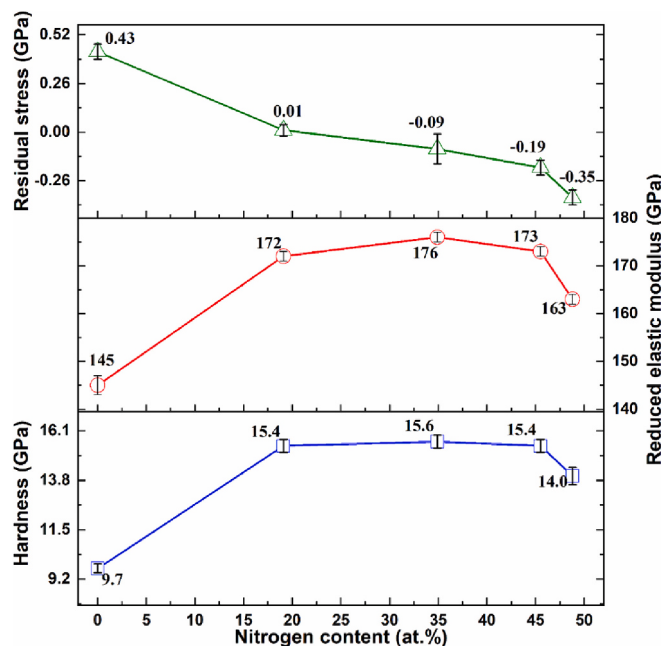


Fig. 8. Relationship between hardness, reduced elastic modulus and nitrogen content of $(\text{TiZrNbSiMo})_{1-x}\text{N}_x$ coatings.

intrinsic stress and coating volume expansion are connected [36]. As the nitrogen content increases from 19.1 to 34.9 at.%, the residual stress of the coatings turns from tensile to compressive and the phase changes from amorphous to nanocrystalline FCC structure. As the nitrogen content is further increased from 34.9 to 48.8 at.%, the compressive residual stress of the FCC-structured coatings increases from -0.09 to -0.35 GPa. According to Lin and coworkers [37], there appears to be an approximately linear relationship between the nitrogen flow rate and residual stress, which is due to the strengthening of the atomic impact effect. Huffman et al. [38] noted that the neutral nitrogen atoms in a mixed N_2/Ar gas predominate in the atomic impact action. Consequently, a larger nitrogen concentration results in a stronger bombardment of the coating by nitrogen atoms, which raises the compressive stress.

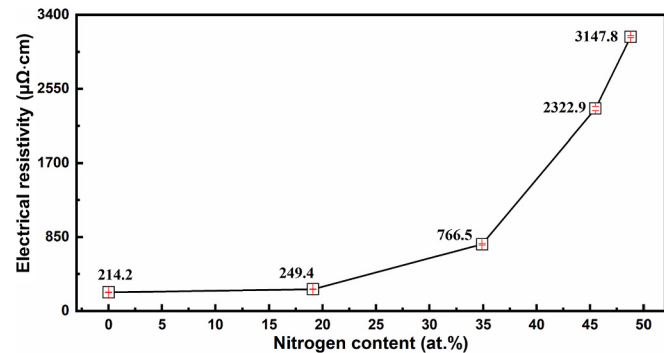


Fig. 9. Electrical resistivity of $(\text{TiZrNbSiMo})_{1-x}\text{N}_x$ HEA coatings.

3.4. Electrical conductivity analysis of $(\text{TiZrNbSiMo})_{1-x}\text{N}_x$ HEA coatings

Fig. 9 and **Table 3** show the electrical resistivity of $(\text{TiZrNbSiMo})_{1-x}\text{N}_x$ HEA coatings. The resistivity value of the nitrogen-free N0 and N2 coatings is low, at approximately $214\text{--}249 \mu\Omega\cdot\text{cm}$, and increases to $766.5 \mu\Omega\cdot\text{cm}$ when the nitrogen content reaches 34.9 at.%(N4). Further an increase of nitrogen to 45.5 at.%(N6), the resistivity rapidly increases to a high value of $2322.9 \mu\Omega\cdot\text{cm}$, and eventually reaches a maximum value of $3147.8 \mu\Omega\cdot\text{cm}$ when the nitrogen content reaches 48.8 at.%(N10). It has been reported that resistivity is often related to vacancies, dislocations and grain boundaries and associated microstructural defects, as well as lattice distortions that contribute to electron scattering [39]. Grain boundary scattering is the primary factor influencing the resistivity of polycrystalline metals, and when grain refinement becomes nanocrystalline, the electron mean free path decreases [40]. Lattice strain in HEAs effectively retards the movement of electrons because severe lattice distortions are induced in them, especially due to differences in atomic size between the alloying elements [41]. In other words, the degree of lattice distortion can affect the electrical resistivity of an alloy [42]. On the other hand, since the electrical resistivity of silicon nitride is ranging from 3.16×10^9 to $1.73 \times 10^{11} \mu\Omega\cdot\text{m}$ [43], the amount of amorphous and high resistivity silicon nitride phase has a very strong influence on the increase of electrical resistivity of coatings. Consequently, $(\text{TiZrNbSiMo})_{1-x}\text{N}_x$ HEA coatings grew more nanocrystalline as the nitrogen concentration increased and also had a larger electrical resistance as a result of the lattice distortion effect and more amount of silicon nitride phase.

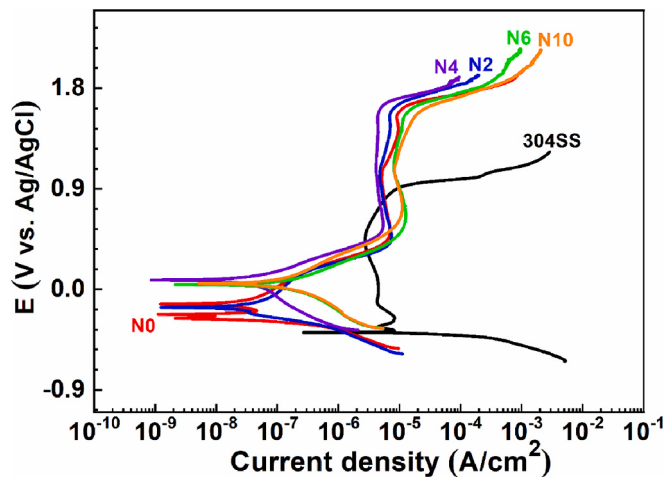


Fig. 10. Potentiodynamic polarization curves of five $(\text{TiZrNbSiMo})_{1-x}\text{N}_x$ coatings and 304SS substrate.

3.5. Corrosion resistance of $(\text{TiZrNbSiMo})_{1-x}\text{N}_x$ HEA coatings

The potentiodynamic polarization curves for 304SS and the five $(\text{TiZrNbSiMo})_{1-x}\text{N}_x$ HEA coatings in 0.5 M H_2SO_4 aqueous solution are presented in Fig. 10. Potentiodynamic polarization curves provide insights into the corrosion performance of each coating, and detailed data on relevant performance are listed in Table 4. Notably, HEA coatings

exhibit a larger passivation range, approximately between 0.86 and 1.14 V, as compared with the narrow range of 0.13 V for 304SS. This indicates that the surface passivation of $(\text{TiZrNbSiMo})_{1-x}\text{N}_x$ HEA coatings offers more effective protection against 0.5 M H_2SO_4 aqueous solution. Additionally, the N4 coatings demonstrate an outstanding corrosion resistance, with an R_p value of $9.71 \times 10^5 \Omega\cdot\text{cm}^2$, which is 610.7 times better than that of 304SS. The I_{corr} values of all $(\text{TiZrNbSiMo})_{1-x}\text{N}_x$ coatings were below $0.067 \mu\text{A}/\text{cm}^2$, which is lower than that of 304SS, $3.316 \mu\text{A}/\text{cm}^2$, indicating their superior corrosion resistance performance. Our previous studies have also highlighted the excellent corrosion resistance of TiZrNbTaFeN [16] high entropy alloy nitride coatings than 304SS in 0.5 M H_2SO_4 aqueous solution. This remarkable corrosion resistance enhances the material's durability in harsh environments, such as the protective coatings on the stainless steel bipolar plates in the PEMFC. After the corrosion test, the corroded surfaces of each $(\text{TiZrNbSiMo})_{1-x}\text{N}_x$ HEA coating and 304SS were further examined using scanning electron microscopy, as depicted in Fig. 11. A severe corroded surface with deep corrosion pits can be seen for the 304SS in Fig. 11(a). On the other hand, very tiny corrosion pit, a very small portion of bulged coatings and cracks are found in Fig. 11(b) to (d) for N4, N6 and N10 coatings. It is well known that the corrosion resistance of a coating is strongly related to its microstructure and defects [44]. The corrosive electrolyte can attack the substrate through the defects and grain boundaries between columnar microstructures of coating. Therefore, the dense and featureless microstructures of $(\text{TiZrNbSiMo})_{1-x}\text{N}_x$ HEA coatings, especially N4, can effectively block the attack of corrosive electrolyte and greatly enhance the corrosion resistance of 304SS substrate.

Table 4

Corrosion characteristics of five $(\text{TiZrNbSiMo})_{1-x}\text{N}_x$ coatings and 304SS substrate tested in 0.5 M H_2SO_4 aqueous solution.

Sample designation	E_{corr} (mV)	I_{corr} ($\mu\text{A}/\text{cm}^2$)	β_a (mV)	β_c (mV)	R_p ($\Omega\cdot\text{cm}^2$)	R_p Ratio	Passivation range (V)
304SS	-378.79	3.316	139.4	13.1	1.59×10^3	1.0	0.12
N0	-249.49	0.026	99.0	123.3	6.81×10^5	428.3	1.14
N2	-160.49	0.023	230.5	99.5	9.05×10^5	569.2	1.13
N4	82.46	0.021	152.0	424.9	9.71×10^5	610.7	1.07
N6	42.95	0.067	208.2	283.4	2.70×10^5	171.7	1.01
N10	51.51	0.061	257	216.2	3.42×10^5	215.1	0.86

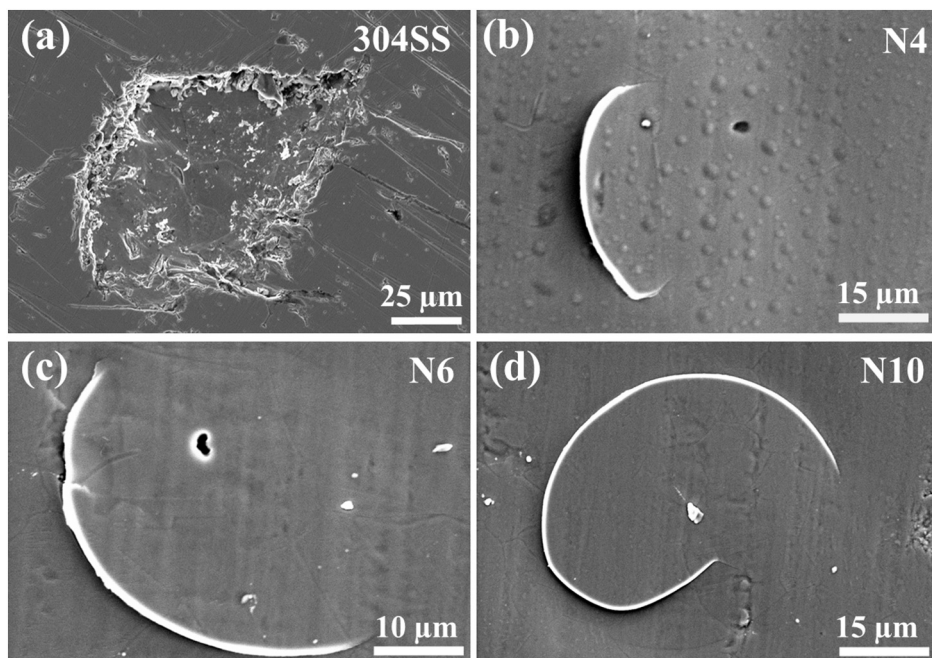


Fig. 11. The surface morphologies of uncoated 304SS substrate, N4, N6 and N10 coatings after corrosion test.

In summary, adjusting nitrogen content of $(\text{TiZrNbSiMo})_{1-x}\text{N}_x$ HEA coatings led to a transition from an amorphous to a nanocrystalline FCC phase structure. The coating hardness initially increased and then decreased with increasing nitrogen content, reaching a peak hardness of 15.6 GPa at a nitrogen content of 34.9 at.%. The FCC-structured $(\text{TiZrNbSiMo})_{1-x}\text{N}_x$ coating with 34.9 at.% nitrogen exhibited the highest corrosion resistance. Additionally, the transformation from the amorphous state to the nanocrystalline FCC state resulted in a sharp rise in electrical resistivity from 214.2 to 766.5 $\mu\Omega\cdot\text{cm}$ and even higher due to the formation of more amount of amorphous silicon nitride phase.

4. Conclusion

In this study, a HiPIMS system was used to deposit TiZrNbSiMo and four $(\text{TiZrNbSiMo})_{1-x}\text{N}_x$ HEA nitride coatings with different nitrogen contents. As the nitrogen flow rate increased from 0 to 10 sccm, the nitrogen content increased from 0 to 48.8 at.%. The HEA coatings exhibited an amorphous structure when the nitrogen content was 19.1 at.% and it transformed into a nanocrystalline FCC phase structure as the nitrogen content was higher than 34.9 at.%. The hardness of HEA coatings increased from 9.7 GPa to a maximum of 15.6 GPa as the nitrogen content increased from 0 to 34.9 at.%. The hardness of coatings gradually decreased to 14.0 GPa as the nitrogen content reached 48.8 at.%. According to the corrosion test in 0.5 M H_2SO_4 aqueous solution, the TiZrNbSiMo and four $(\text{TiZrNbSiMo})_{1-x}\text{N}_x$ HEA nitride coatings can enhance the corrosion resistance of bare 304SS substrate because of their dense microstructure. The FCC-structured $(\text{TiZrNbSiMo})_{1-x}\text{N}_x$ nitride coating with a nitrogen content of 34.9 at.% and an electrical resistivity of 766.5 $\mu\Omega\cdot\text{cm}$ had the highest corrosion resistance, which was $9.71 \times 10^5 \Omega\cdot\text{cm}^2$, around 670.1 times higher than that of uncoated 304SS substrate. We suggested that the 34.9 at.% nitrogen contained TiZrNbSiMoN nitride coating had a promising application as the protective layer on the stainless steel bipolar plates in proton exchange membrane fuel cells.

CRediT authorship contribution statement

Bih-Show Lou: Supervision, Methodology, Funding acquisition. **Ren-Zong Lin:** Investigation. **Chia-Lin Li:** Writing – original draft, Data curation. **Jyh-Wei Lee:** Writing – review & editing, Supervision, Resources, Methodology, Funding acquisition.

Declaration of competing interest

The authors declare that they have no known competing financial interests or personal relationships that could have appeared to influence the work reported in this paper.

Acknowledgement

The authors would like to acknowledge funding given by the National Science and Technology Council (NSTC) in Taiwan under Project Nos. NSTC 110-2221-E-131-004-MY3 and NSTC 112-2221-E-182-022. The financial support from the Chang Gung Memorial Hospital, Taiwan, through Contract No. CMRPD5M0021 to B. S. Lou is also acknowledged. This work was also financially supported by the “High Entropy Materials Center” from The Featured Areas Research Center Program within the framework of the Higher Education Sprout Project by the Ministry of Education (MOE) in Taiwan.

References

- [1] J.-W. Yeh, S.-K. Chen, S.-J. Lin, J.-Y. Gan, T.-S. Chin, T.-T. Shun, C.-H. Tsau, S.-Y. Chang, Nanostructured high-entropy alloys with multiple principal elements: novel alloy design concepts and outcomes, *Adv. Eng. Mater.* 6 (2004) 299–303.
- [2] B. Cantor, I.T.H. Chang, P. Knight, A.J.B. Vincent, Microstructural development in equiatomic multicomponent alloys, *Mater. Sci. Eng. A* 375–377 (2004) 213–218.
- [3] M. Gupta, R. Musalek, T. Tesar, Microstructure and failure analysis of suspension plasma sprayed thermal barrier coatings, *Surf. Coat. Technol.* 382 (2020) 125218.
- [4] M. Łapiński, M. Walas, A. Gapska, D. Kulik, A. Szmytko, P. Twardowski, W. Sadowski, B. Kościelska, Structure and optical parameters of Eu doped tellurium oxide thin films prepared by reactive magnetron sputtering method, *Thin Solid Films* 691 (2019) 137592.
- [5] M. Zhang, X. Zhou, X. Yu, J. Li, Synthesis and characterization of refractory TiZrNbWMo high-entropy alloy coating by laser cladding, *Surf. Coat. Technol.* 311 (2017) 321–329.
- [6] P.-K. Huang, J.-W. Yeh, Effects of nitrogen content on structure and mechanical properties of multi-element (AlCrNbSiTiV)N coating, *Surf. Coat. Technol.* 203 (2009) 1891–1896.
- [7] C. Guo, S. Yi, R. Si, B. Xi, X. An, J. Liu, J. Li, S. Xiong, Advances on defect engineering of vanadium-based compounds for high-energy aqueous zinc-ion batteries, *Adv. Energy Mater.* 12 (2022) 2202039.
- [8] W.-J. Shen, M.-H. Tsai, J.-W. Yeh, Machining performance of sputter-deposited (Al0.34Cr0.22Nb0.11Si0.11Ti0.22)50N50 high-entropy nitride coatings, *Coatings* 5 (2015) 312–325.
- [9] H.-T. Hsueh, W.-J. Shen, M.-H. Tsai, J.-W. Yeh, Effect of nitrogen content and substrate bias on mechanical and corrosion properties of high-entropy films (AlCrSiTiZr)100-xN_x, *Surf. Coat. Technol.* 206 (2012) 4106–4112.
- [10] X.H. Yan, J.S. Li, W.R. Zhang, Y. Zhang, A brief review of high-entropy films, *Mater. Chem. Phys.* 210 (2018) 12–19.
- [11] C.-H. Lai, S.-J. Lin, J.-W. Yeh, S.-Y. Chang, Preparation and characterization of AlCrTaTiZr multi-element nitride coatings, *Surf. Coat. Technol.* 201 (2006) 3275–3280.
- [12] C. Zhang, X. Lu, C. Wang, X. Sui, Y. Wang, H. Zhou, J. Hao, Tailoring the microstructure, mechanical and tribocorrosion performance of (CrNbTiAlV)N high-entropy nitride films by controlling nitrogen flow, *J. Mater. Sci. Technol.* 107 (2022) 172–182.
- [13] H. Li, N. Jiang, J. Li, J. Huang, J. Kong, D. Xiong, Hard and tough (NbTaMoWN)_x high entropy nitride films with sub-stoichiometric nitrogen, *J. Alloys Compd.* 889 (2021) 161713.
- [14] B.-S. Lou, C.-J. Wang, Y.-Y. Chen, S.-B. Hung, Y.-C. Lin, J.-W. Lee, Phase, mechanical property and corrosion resistance evaluation of W-Nb-ta-Ti and W-Nb-ta-Ti-N medium entropy alloy thin films, *Surf. Coat. Technol.* 442 (2022) 128339.
- [15] N. Ravi, R. Markandeya, S.V. Joshi, Effect of nitrogen pressure on mechanical properties of nc-TiAlN/a-Si₃N₄ nanocomposite coatings deposited by cathodic arc PVD process, *Mater. Today Proc.* 3 (2016) 3002–3011.
- [16] S. Bachani, C.-J. Wang, B. Lou, L.-C. Chang, J.-W. Lee, Fabrication of TiZrNbTaFeN high-entropy alloys coatings by HiPIMS: effect of nitrogen flow rate on the microstructural development, mechanical and tribological performance, electrical properties and corrosion characteristics, *J. Alloys Compd.* 873 (2021) 159605.
- [17] W. Xu, M. Liao, X. Liu, L. Ji, P. Ju, H. Li, H. Zhou, J. Chen, Microstructures and properties of (TiCrVAl)N high entropy ceramics films by multi-arc ion plating, *Ceram. Int.* 47 (2021) 24752–24759.
- [18] A. Xia, R. Dedoncker, O. Glushko, M. Cordill, D. Depla, R. Franz, Influence of the nitrogen content on the structure and properties of MoNbTaVW high entropy alloy thin films, *J. Alloys Compd.* 850 (2020) 156740.
- [19] J.-W. Lee, C.-Y. Chen, Y.-J. Chen, C.-H. Tzeng, Y.-I. Chen, Effects of nitrogen flow ratio on the structural, mechanical, and anticorrosive properties of co-sputtered (NbTaMoWN)_x films, *J. Mater. Res. Technol.* 21 (2022) 1890–1902.
- [20] J. Li, Y. Chen, Z. Yiman, X. Shi, S. Wang, S. Zhang, Super-hard (MoSi₃TiV₂Zr)N_x high-entropy nitride coatings, *J. Alloys Compd.* 926 (2022) 166807.
- [21] P. Cui, W. Li, P. Liu, K. Zhang, F. Ma, X. Chen, R. Feng, P.K. Liaw, Effects of nitrogen content on microstructures and mechanical properties of (AlCrTiZrHf)N high-entropy alloy nitride films, *J. Alloys Compd.* 834 (2020) 155063.
- [22] L. Chen, W. Li, P. Liu, K. Zhang, F. Ma, X. Chen, H. Zhou, X. Liu, Microstructure and mechanical properties of (AlCrTiZrVN)_x high-entropy alloy nitride films by reactive magnetron sputtering, *Vacuum* 181 (2020) 109706.
- [23] O. Maksakova, O. Bondar, K. Belovol, V.M. Beresnev, O. Sobol, S.S. Grankin, V. Novikov, D. Yeskermessov, Physical and Mechanical Properties of (Ti-Zr-Nb)N Coatings, Fabricated by Vacuum-Arc Deposition, 2015.
- [24] V. Braic, A. Vladescu, M. Balaceanu, C.R. Luculescu, M. Braic, Nanostructured multi-element (TiZrNbHfTa)N and (TiZrNbHfTa)C hard coatings, *Surf. Coat. Technol.* 211 (2012) 117–121.
- [25] F. Bi, L. Peng, P. Yi, X. Lai, Multilayered Zr-C-a-C film on stainless steel 316L as bipolar plates for proton exchange membrane fuel cells, *J. Power Sources* 314 (2016) 58–65.
- [26] W. Yan, Y. Zhao, Y. Zhang, Q. Li, S. Chen, H. Yuan, Z. Zhang, L. Chen, J. Luo, P. Pang, G. He, M. Ying, B. Liao, Corrosion-resistant and interfacial conductive AlTiVCrMo high-entropy alloy and (AlTiVCrMo)N_x high-entropy ceramics coatings for surface modification of bipolar plates in proton exchange membrane fuel cells, *J. Power Sources* 527 (2022) 231217.
- [27] A.P. Ehiasarian, A. Vetushta, Y.A. Goncalvo, G. Sáfrán, L. Székely, P.B. Barna, Influence of high power impulse magnetron sputtering plasma ionization on the microstructure of TiN thin films, *J. Appl. Phys.* 109 (2011) 104314.
- [28] Y. Yuan, L. Yang, Z. Liu, Q. Chen, High power impulse magnetron sputtering and its applications, *Plasma Sci. Technol.* 20 (2018) 065501.
- [29] K. Sarakinos, J. Alami, S. Konstantinidis, High power pulsed magnetron sputtering: a review on scientific and engineering state of the art, *Surf. Coat. Technol.* 204 (2010) 1661–1684.
- [30] G.G. Stoney, C.A. Parsons, The tension of metallic films deposited by electrolysis, *Proc. R. Soc. Lond. Ser. Contain. Pap. Math. Phys. Character* 82 (1997) 172–175.
- [31] W.A. Brantley, Calculated elastic constants for stress problems associated with semiconductor devices, *J. Appl. Phys.* 44 (1973) 534–535.

- [32] J.W. Yeh, Y.L. Chen, S.J. Lin, S.K. Chen, High-entropy alloys – a new era of exploitation, *Mater. Sci. Forum* 560 (2007) 1–9.
- [33] J.-W. Lee, S.-T. Chang, H.-W. Chen, C.-H. Chien, J.-G. Duh, C.-J. Wang, Microstructure, mechanical and electrochemical properties evaluation of pulsed DC reactive magnetron sputtered nanostructured Cr-Zr-N and Cr-Zr-Si-N thin films, *Surf. Coat. Technol.* 205 (2010) 1331–1338.
- [34] Y.-C. Kuo, C.-J. Wang, J.-W. Lee, The microstructure and mechanical properties evaluation of CrTiAlSiN coatings: effects of silicon content, *Thin Solid Films* 638 (2017) 220–229.
- [35] S.-Y. Chang, S.-Y. Lin, Y.-C. Huang, C.-L. Wu, Mechanical properties, deformation behaviors and interface adhesion of $(\text{AlCrTaTiZr})\text{N}_x$ multi-component coatings, *Surf. Coat. Technol.* 204 (2010) 3307–3314.
- [36] H. Oettel, R. Wiedemann, Residual stresses in PVD hard coatings, *Surf. Coat. Technol.* 76–77 (1995) 265–273.
- [37] Y.-C. Lin, S.-Y. Hsu, Y.-T. Lai, P.-H. Kuo, S.-Y. Tsai, J.-G. Duh, Effect of the $\text{N}_2/(\text{Ar}+\text{N}_2)$ ratio on mechanical properties of high entropy nitride $(\text{Cr}_{0.35}\text{Al}_{0.25}\text{Nb}_{0.12}\text{Si}_{0.08}\text{V}_{0.20})\text{N}_x$ films, *Mater. Chem. Phys.* 274 (2021) 125195.
- [38] G.L. Huffman, D.E. Fahline, R. Messier, L.J. Pilione, Stress dependence of reactively sputtered aluminum nitride thin films on sputtering parameters, *J. Vac. Sci. Technol. Vac. Surf. Films* 7 (1989) 2252–2255.
- [39] Y. Zhang, G.M. Stocks, K. Jin, C. Lu, H. Bei, B.C. Sales, L. Wang, L.K. Béland, R. E. Stoller, G.D. Samolyuk, M. Caro, A. Caro, W.J. Weber, Influence of chemical disorder on energy dissipation and defect evolution in concentrated solid solution alloys, *Nat. Commun.* 6 (2015) 8736.
- [40] R. Bel Hadj Tahar, T. Ban, Y. Ohya, Y. Takahashi, Tin doped indium oxide thin films: electrical properties, *J. Appl. Phys.* 83 (1998) 2631–2645.
- [41] W. Huo, X. Liu, S. Tan, F. Fang, Z. Xie, J. Shang, J. Jiang, Ultrahigh hardness and high electrical resistivity in nano-twinned, nanocrystalline high-entropy alloy films, *Appl. Surf. Sci.* 439 (2018) 222–225.
- [42] X. Feng, J. Zhang, Z. Xia, W. Fu, K. Wu, G. Liu, J. Sun, Stable nanocrystalline NbMoTaW high entropy alloy thin films with excellent mechanical and electrical properties, *Mater. Lett.* 210 (2018) 84–87.
- [43] O.A. Lukianova, A.N. Khmara, S.N. Perevislov, D.A. Kolesnikov, V.V. Krasilnikov, Electrical resistivity of silicon nitride produced by various methods, *Ceram. Int.* 45 (2019) 9497–9501.
- [44] S.-B. Hung, C.-J. Wang, Y.-Y. Chen, J.-W. Lee, C.-L. Li, Thermal and corrosion properties of V-Nb-Mo-ta-W and V-Nb-Mo-Ta-W-Cr-B high entropy alloy coatings, *Surf. Coat. Technol.* 375 (2019) 802–809.